Design of an Anti-Misalignment Coil With Hilbert Structure for WPT System

Zhiying Zheng, Zhihao Ye, Changcheng Zhao, Cheng Chen, and Qijun Deng

***Abstract*—Currently, coil misalignment is recognized as one of the primary factors limiting the transmission efficiency of wireless power transfer (WPT) systems, presenting a substantial barrier to the large-scale adoption of WPT. To enhance transmission efficiency under misalignment, mitigate the impacts of misalignment, and increased transmission distance of WPT systems, research on Hilbert fractal curves in related fields was referenced, mutual inductance expressions for coils with Hilbert-extended structures and conventional coils were derived based on their mathematical formulations, and the potential advantages of Hilbert curves in wireless power transfer applications were analyzed. Supported by extensive simulation outcomes, a fractal coil incorporating a Hilbert structure was designed without altering coil manufacturing costs. The transmission performance advantages of this coil were investigated through simulations. A WPT system verification platform utilizing an *LCC-S* circuit was constructed, where 300 W power and efficiency tests were conducted under relatively consistent zero voltage switch (ZVS) conditions for both coil types. Experimental results across varying transmission distances and misalignment distances were obtained. The results demonstrate that the proposed coils comprehensively optimize the power transfer capability of conventional coils, delivering more stable output power and improving the transmission efficiency by over 10% (up to 24%).**

***Index Terms*—Magnetic coupling mechanism (MCM), misalignment performance, wireless power transmission (WPT).**

I. Introduction

MAGNETIC coupling wireless power transfer (MCWPT) is a research hotspot that has emerged in recent years. Compared with traditional forms of power transmission, MCWPT is more convenient, safe and reliable, and has therefore been widely used in fields, such as electric vehicles (EVs), medical care and smart home appliances [1], [2], [3]. However, the efficiency of WPT system can be obviously reduced by the misalignment of the coil, which has a significant impact on the application of WPT system [4], [5], [6]. In wireless charging applications for EVs, the transmission distance (TD) between the receiving coil within the chassis of different vehicle models and the ground-based transmitting coil, as well as the offset distance (OD) during parking, can significantly affect charging efficiency, resulting in substantial energy waste.

How to improve the anti-misalignment ability of the coil, optimizing the mutual inductance between the magnetic coupling mechanisms (MCMs) under misalignment, and improve the energy transfer efficiency (TE) is of great significance for the research of WPT systems [7].

Up to now, many scholars have conducted a large number of studies on the anti-misalignment capability of MCM. Their research has focused on two main areas: optimizing the compensation circuit structure and matching control strategies [8], [9], [10], [11], [12], [13] or optimizing the structure of the MCM. From one perspective, the latter is obviously more convenient and effective than the former. There are various types of optimization of the MCM structure. One is the use of repeaters: Zhao et al. [14] added a relay coil (RC) outside the coil to achieve an efficiency improvement of about 3%. Rong et al. [15] designed a set of passive matrix coils with genetic algorithms as repeaters, which effectively improved the transmission efficiency when the coil was misalignment over medium distances. However, this type of coil relies on a coil group with a more complex structure than the coil itself and introduces an additional control link. The second is to optimize the layout of the transmitting and receiving coils [16], [17], [18], [19], [20], [21], [22]. Although these methods all use different coil arrangements to improve the system's misalignment resistance and TE, their improvement relies on additional coils, which obviously increases the cost of MCM. In particular, the coil structure based on a rectangular structure is single, and the question of how to minimize the change and most effectively improve the offset resistance of the WPT system while maintaining the cost of existing coil design and the basic coil structure is currently a gap in the research on the structure of MCM.

Wolf and Shmilovitz [23] proposed that changing the geometry of the coil can effectively reduce magnetic losses during transmission. Traditional MCMs often use a simple coil design, which limits the TD and TE of the energy. Therefore, an optimized design for the MCM has a direct impact on TD, TE, and misalignment resistance of the system.

Under this background, numerous current studies have focused on investigating the geometric shapes of coils in MCMs to improve the transmission performance of WPT systems at minimal cost. Li et al. [24] proposed an asymmetric and reverse

Received 30 July 2025; revised 16 September 2025; accepted 24 October 2025. Date of publication 14 November 2025; date of current version 19 January 2026. This work was supported by the National Key R & D Program of China (Key Special Project for Marine Environmental Security and Sustainable Development of Coral Reefs 2022-3.1). Recommended for publication by Associate Editor M. Ponce-Silva. *(Corresponding author: Cheng Chen.)*

Zhiying Zheng, Zhihao Ye, Changcheng Zhao, and Cheng Chen are with the Naval University of Engineering, Wuhan 430030, China (e-mail: m24180802@nue.edu.cn; 1920191216@nue.edu.cn; m24180812@nue.edu.cn; chencheng_wpt@whu.edu.cn).

Qijun Deng is with the Hubei Key Laboratory of Power Equipment & System Security for Integrated Energy, School of Electrical Engineering and Automation, Wuhan University, Wuhan 430072, China (e-mail: dqj@whu.edu.cn).

Color versions of one or more figures in this article are available at https://doi.org/10.1109/TPEL.2025.3630264.

Digital Object Identifier 10.1109/TPEL.2025.3630264

series coil (ARSC), which enables the receive coil to comprise two coils of different sizes, facilitating stable power input for EVs during movement. Li et al. [25] also introduced a tian-font magnetic shielding and anti-series active coil, significantly reducing the cost of the ferromagnetic materials compared to conventional coils and shielding structures of equivalent dimensions. YADAV and VEERACHARY enhanced the receive coil structure using a three-level coil, achieving lateral misalignment tolerance up to 30% of the coil size within a 5% error margin [26]. Zhang et al. [27] skillfully utilized the boundaries of four circular coils to realize a focusing effect on the central magnetic field, thereby improving the misalignment tolerance of MCMs to some extent. However, these designs still adhere to traditional combinations and arrangements of rectangular coil structures, lacking creative alterations to the coil body itself and failing to break through conventional concepts for bold innovations.

Hilbert fractals are known for their excellent space-filling properties and have a solid research foundation in antenna manufacturing, capacitor development and the field of sensors. For example, the gas sensor is designed as a Hilbert fractal structure, which uses the large specific surface area of fractal geometry to achieve efficient information collection [28]. Tian et al. [29] designed a planar antenna based on Hilbert curves, and the research proved that this antenna has good stability when dealing with deformation and discharge tests. Wang et al. [30] and Xu and Hei [31], applied Hilbert fractals as a sensor design with excellent performance in the field of corona detection. Ali et al. [32] designed a microwave sensor using Hilbert fractals, which exhibited the characteristics of low cost, small usage of space and high sensitivity. It is worth mentioning that Yousefi and Ramah [33] improved the magnetic core structure by using Hilbert fractals, which increased the coil coupling factor while reducing costs. This provides some reference value for the application of Hilbert fractals in MCM.

This article converges advancements in MCM structural design and Hilbert curve application through a systematic integration framework, establishing a cross-domain methodology for enhanced wireless charging system optimization. On the basis of the traditional coil arrangement structure, some of the wires, in the form of Hilbert curves, fill the coil plane, which effectively improves the anti-misalignment performance of the coil and also improves the TE over longer distances.

The innovations of this article are as follows.

1) Without changing the area of the coil plane or the length of wire, TE of the WPT system is effectively improved when the coil is subjected to a large offset at close range.
2) Without changing the area of the coil plane or the length of the wire, overall TE of the WPT system is improved when the TD is slightly increased.
3) The physical properties of the designed coil are similar to those of traditional coils. Minimal changes have been made while maintaining the original structure, which maximizes its performance.
4) The advantages of Hilbert curves in other electromagnetic fields have been applied to WPT systems.

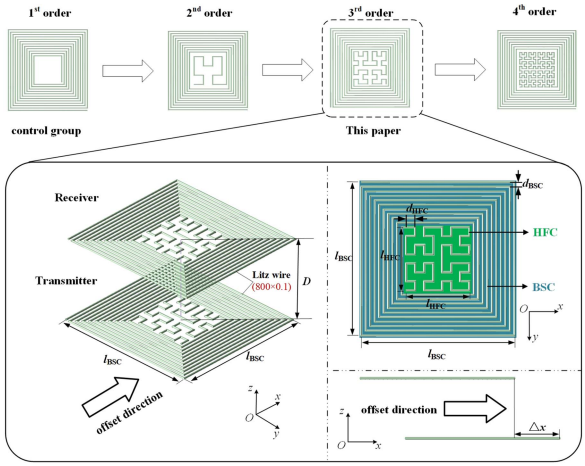

Fig. 1. Overview and evolution of the proposed coil.

TABLE I
RELATED PARAMETERS FOR DESIGN EXAMPLES

symbol	value	symbol	value
l_{BSC}	340 mm	D	120-200 mm
l_{HFC}	140 mm	f	120 kHz
d_{BSC}	10 mm	offset distance	0-204 mm
d_{HFC}	20 mm	Total length of coil	11260 mm

II. EXAMPLE OF THE DESIGN OF COIL

According to previous studies [29], [30], [32], [33], the Hilbert fractal exhibits good performance in capturing electromagnetic signals due to its excellent spatial filling capacity. In addition, research has shown that the Hilbert fractal can generate a more uniform magnetic field.

The coil structure designed in this article with a Hilbert expansion structure and its evolutionary process are shown in Fig. 1. The coil mainly consists of two parts: a basic square coil (BSC) and a Hilbert fractal coil (HFC). Two coils with the same BSC and HFC structures together form the transmitter and receiver of the MCM. In this design example, the coils are wound with 0.1 mm $*$ 800 litz wire. The BSC contour side length $l_{\mathrm{BSC}} = 340$ mm, the fractal coil (FC) contour side length $l_{\mathrm{HSC}} = 140$ mm, BSC turn spacing $d_{\mathrm{BSC}} = 10$ mm, the side length of HFC basic unit $d_{\mathrm{HSC}} = 20$ mm. The research in this article will focus on the anti-misalignment performance in the X-axis direction in the coil plane. The specific parameters of this paper are shown in Table I.

A. Mathematical Principle of Hilbert Curve

The evolution of the Hilbert coil is also illustrated in Fig. 1, where the coil is modeled from left to right with HFC of orders 1 to 4. Its initial graph is a square contour with one side missing, and subsequently this curve is recursively divided to fill the region using a quadrature pattern, and its evolution can be described as follows: Let the region be a square with side length l. The 1st order curve is an unclosed curve sequentially linking the centers of small squares with side length $l/2$, and thus the nth order curve is an unclosed curve sequentially linking the

centers of small squares with side length $1/2^n$, and the graphical region of the The first and second quadrants are the same as the $(n-1)$st order curve, and the third and fourth quadrants are formed by rotating the $(n-1)$st order curve by 90° clockwise and counterclockwise, respectively.

This characteristic represents one of the significant manifestations of the self-similarity inherent in Hilbert fractals. Based on this characteristic, Hausdorff dimension D_{H} is employed in mathematics to characterize the properties of fractal patterns

$$D_{\mathrm{H}} = \frac{\ln 4}{\ln 2} = 2. \tag{1}$$

The findings demonstrate that Hilbert curves exhibit 2-D characteristics when filling space. Consequently, the fractal normalization expression can be mapped from 1-D to 2-D

$$H(t) : [0,1] \to [0,1]^2. \tag{2}$$

Moreover, expressing it parametrically, the first-order Hilbert curve comprises three linear segments with the following parametric expressions:

$$H_1(t) \begin{cases} \left(\frac{t}{2}, \frac{t}{2}\right), t \in [0, \frac{1}{3}] \\ \left(\frac{1}{2}\left(t-\frac{1}{3}\right)+\frac{1}{2}, \frac{1}{2}\left(t-\frac{1}{3}\right)+\frac{1}{2}\right), t \in [\frac{1}{3}, \frac{2}{3}] \\ \left(\frac{1}{2}(1-t)+\frac{1}{2}, \frac{1}{2}(1-t)\right), t \in [\frac{2}{3}, 1]. \end{cases} \tag{3}$$

Furthermore, by regarding $H_n(t)$ as a configuration comprising four $H_{n-1}(t)$ subcurves via mathematical induction, the following expression can be derived:

$$H_n(t) \begin{cases} \left(\frac{y_{n-1}(4t)}{2}, \frac{x_{n-1}(4t)}{2}\right), t \in [0, \frac{1}{4}] \\ \left(\frac{x_{n-1}(4t-1)}{2}, \frac{y_{n-1}(4t-1)+1}{2}\right), t \in [\frac{1}{4}, \frac{1}{2}] \\ \left(\frac{x_{n-1}(4t-2)+1}{2}, \frac{y_{n-1}(4t-2)+1}{2}\right), t \in [\frac{1}{2}, \frac{3}{4}] \\ \left(\frac{2-y_{n-1}(4t-3)}{2}, \frac{1-x_{n-1}(4t-3)}{2}\right), t \in [\frac{3}{4}, 1] \end{cases} \tag{4}$$

in which $(x_{n-1}(t), y_{n-1}(t)) = H_{n-1}(t)$

In each recursive iteration, the Hilbert curve subdivides the parameter interval [0, 1] into 4^n segments, with each segment corresponding to a spatial step size of $\frac{1}{2^n}$, thereby yielding the Hölder exponent $\alpha = \frac{1}{2}$.

Which presents

$$\| H(t) - H(t') \| \leq C \cdot | t - t' |^{1/2}. \tag{5}$$

In this expression, C denotes a constant.

The Hölder exponent α significantly impacts magnetic field homogeneity: A lower Hölder exponent indicates higher curve roughness, which induces magnetic vortices in the field. This phenomenon enhances near-field coupling but simultaneously increases far-field flux leakage. Conversely, a higher Hölder exponent yields coil behavior closer to conventional patterns, resulting in more concentrated magnetic field distribution—albeit with greater sensitivity to positional offsets. The intermediate value $\alpha = 0.5$ represents a favorable compromise engineered by Hilbert fractals to balance these performance metrics.

To further investigate these characteristics, an equivalent circuit model will be established for mutual inductance (M) analysis.

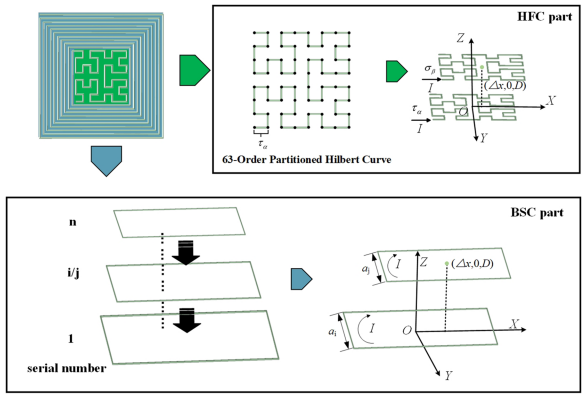

Fig. 2. Coil mutual inductance equivalent analysis process proposed in this article.

For analytical convenience regarding the coil proposed in this work, the hybrid coil can be decomposed into HFC and BSC components according to the configuration illustrated in Fig. 2.

To further investigate mutual inductance, the BSC—a rectangular coil with m turns—can be approximated as m superimposed square coils (SCs) of specific side lengths.

Proceeding with this model, consider the ith transmitter coil S_{i} and jth receiver coil S_{j}. With the transmitter centered at the origin and the receiver displaced by Δx along the x-axis, its center coordinates are (Δx, 0, D). Given sides a_i and a_j, respectively, the mutual inductance is derived via Neumann's formula

$$M_{\mathrm{ij}} = {N_1}^2 \frac{\mu_0}{4\pi} \oint_{S_{\mathrm{i}}} \oint_{S_{\mathrm{j}}} \frac{dl_{\mathrm{i}} \cdot dl_{\mathrm{j}}}{r} \tag{6}$$

where N_1 denotes litz wire turns, dl_{i} and dl_{j} represent infinitesimal elements, and r indicates the distance between these differential elements. Further leveraging symmetry from rectangular topology and axial offset configuration

$$M_{\mathrm{ij}} = \frac{\mu_0 {N_1}^2}{4\pi}(2\alpha - 2\beta + \gamma_1 - \gamma_2 - \gamma_3 + \gamma_4) \tag{7}$$

in which

$$\alpha = \int_{-\frac{a_i}{2}}^{\frac{a_i}{2}} \int_{x_1-\frac{a_j}{2}}^{x_1+\frac{a_j}{2}} \frac{dx_i \cdot dx_j}{\sqrt{(x_i - x_j)^2 + \left(\frac{a_i - a_j}{2}\right)^2 + d^2}}$$

$$\beta = \int_{-\frac{a_i}{2}}^{\frac{a_i}{2}} \int_{x_1-\frac{a_j}{2}}^{x_1+\frac{a_j}{2}} \frac{dx_i \cdot dx_j}{\sqrt{(x_i - x_j)^2 + \left(\frac{a_i + a_j}{2}\right)^2 + d^2}}$$

$$\gamma_1 = \int_{-\frac{a_i}{2}}^{\frac{a_i}{2}} \int_{-\frac{a_j}{2}}^{\frac{a_j}{2}} \frac{dy_i \cdot dy_j}{\sqrt{\left[\frac{a_i}{2} - \left(x_i + \frac{a_{\mathrm{j}}}{2}\right)\right]^2 + (y_i - y_j)^2 + d^2}}$$

$$\gamma_2 = \int_{-\frac{a_i}{2}}^{\frac{a_i}{2}} \int_{-\frac{a_j}{2}}^{\frac{a_j}{2}} \frac{dy_i \cdot dy_j}{\sqrt{\left[\frac{a_i}{2} - \left(x_i - \frac{a_{\mathrm{j}}}{2}\right)\right]^2 + (y_i - y_j)^2 + d^2}}$$

$$\gamma_3 = \int_{-\frac{a_i}{2}}^{\frac{a_i}{2}} \int_{-\frac{a_j}{2}}^{\frac{a_j}{2}} \frac{dy_i \cdot dy_j}{\sqrt{\left[-\frac{a_i}{2} - \left(x_i + \frac{a_j}{2}\right)\right]^2 + (y_i - y_j)^2 + d^2}}$$

$$\gamma_4 = \int_{-\frac{a_i}{2}}^{\frac{a_i}{2}} \int_{-\frac{a_j}{2}}^{\frac{a_j}{2}} \frac{dy_i \cdot dy_j}{\sqrt{\left[-\frac{a_i}{2} - \left(x_i - \frac{a_j}{2}\right)\right]^2 + (y_i - y_j)^2 + d^2}}.$$

Consequently, the mutual inductance for the rectangular coil section can be expressed as

$$M_{\mathrm{S}} = \sum_{i=1}^{m} \sum_{j=1}^{m} M_{\mathrm{i}}. \tag{8}$$

The mutual inductance of the HFC is denoted by M_H, yielding

$$M = M_{\mathrm{S}} + M_{\mathrm{H}} + M_{\mathrm{SH}} + M_{\mathrm{HS}}. \tag{9}$$

For the FC, normalized expressions are given based on (4), where the coil is divided into 63 equal-length segments

$$\begin{cases} \tau = \frac{\alpha}{63},\ \alpha = 0, 1, 2 \ldots 63 \\ \sigma = \frac{\beta}{63},\ \beta = 0, 1, 2 \ldots 63. \end{cases} \tag{10}$$

Following the generalized Neumann formula, this yields:

$$M_H = \frac{{N_1}^2 {l_{\mathrm{HFC}}}^2 \mu_0}{4\pi} \sum_{\alpha=0}^{63} \sum_{\beta=0}^{63} K \tag{11}$$

in which

$$K = \frac{\nabla H(\tau) \cdot \nabla H(\sigma)}{||l_{\mathrm{HFC}}(H(\tau) - H(\sigma)) + (\Delta x, 0, D)||}.$$

Based on the established computational methods for M_{H} and M_{S} and their mutual inductance physical interpretation, it follows that:

$$M_{\mathrm{HSj}} = \frac{\mu_0 {N_1}^2}{4\pi} \sum_{\alpha=0}^{63} \sum_{\mathrm{p}=0}^{3} \frac{(x_{\mathrm{p}}, y_{\mathrm{p}}) \cdot l_{\mathrm{HFC}} H(\tau)}{||(x_{\mathrm{p}}, y_{\mathrm{p}}) - l_{\mathrm{HFC}} H(\tau)||} \tag{12}$$

where x_{p} and y_{p} represent the center coordinates of each side of the square, and M_{HSj} corresponds to the SC with side length a_{j}. By extension

$$M_{\mathrm{SHi}} = \frac{\mu_0 {N_1}^2}{4\pi} \sum_{\beta=0}^{63} \sum_{\mathrm{q}=0}^{3} \frac{(x_{\mathrm{q}}, y_{\mathrm{q}}) \cdot l_{\mathrm{HFC}} H(\sigma)}{||(x_{\mathrm{q}}, y_{\mathrm{q}}) - l_{\mathrm{HFC}} H(\sigma)||} \tag{13}$$

where x_{q} and y_{q} denote the center coordinates for each side of the SC, while M_{SHi} corresponds to the SC having side length a_{i}.

The overall mutual inductance follows as the summation:

$$M = \sum_{i=1}^{m} \sum_{j=1}^{m} M_{\mathrm{ij}} + M_{\mathrm{H}} + \sum_{i=1}^{m} M_{\mathrm{SHi}} + \sum_{j=1}^{m} M_{\mathrm{HSj}}. \tag{14}$$

Derived from the analytical relationships presented, mutual inductance M is fundamentally a function of parameters m, Δx, and D, mathematically represented as $M(m, \Delta x, D)$. Due to the prohibitively complex formulation of this expression, advanced finite element analysis tools are required for subsequent model implementation and simulation.

The intrinsic recursive property of Hilbert curves, combined with Hölder exponent analysis, demonstrates their capacity for high-density conductor positioning within confined areas. This configuration notably enhances the intercoil flux linkage, thereby maximizing mutual inductance M.

Similarly, the self-inductance of a rectangular coil is typically approximated using a modified Wheeler's formula

$$L \approx \frac{G_1 \mu_0 N_1^2 l_{\mathrm{avg}}}{1 + G_2 \rho} \left[1 - \frac{r_0}{l_{\mathrm{avg}}} \left(\frac{2}{\pi} \ln\left(\frac{4 l_{\mathrm{avg}}}{r_0}\right) - \frac{1}{2}\right)\right] \tag{15}$$

in which

$l_{\mathrm{avg}} \approx \frac{l_{\max} + l_{\min}}{2}$ (where these two variables represent the maximum and minimum side lengths of the coil, respectively), $\rho = \frac{l_{\max} - l_{\min}}{l_{\max} + l_{\min}}$ denotes the coil fill factor and r_0 denotes the wire diameter. G_1 and G_2 represent the coil geometric constant (for SC, $G_1 = 2.34$, $G_2 = 2.75$).

The self-inductance calculation for coils with fractal structures can adopt the same method as mutual inductance computation: first calculate the self-inductance of peripheral auxiliary coils, then determine the self-inductance of the fractal structure and their summation, expressed as

$$L_{\mathrm{H}} = L_{\mathrm{S}} + L_{\mathrm{HFC}} + M_{\mathrm{SHFC}}. \tag{16}$$

It is also worth noting that the dense folding of the Hilbert curve may reduce the susceptibility to external EMI by impairing each other out through local magnetic fields. However, the complexity of the fractal structure also tends to complicate the magnetic field of the wire in space, and thus further research is needed to overcome the losses, which requires further optimisation of the fractal structure.

B. Construction Process of HFC Structure

When the wire length is fixed, the order n and the length of basic unit d_{HFC} together determine the proportion of HFC in the entire coil.

When studying a traditional rectangular coil, broadly speaking, we can regard the innermost one turn of wire as a HFC of order 1, while the outer $N - 1$ turns of wire form a BSC structure. The characteristic of Hilbert curves is their ability to fill space in higher dimensions as 1-D shapes. The higher order of the Hilbert curve, the better its ability to fill space [30]. Therefore, it is not difficult to conclude that, on the one hand, when the fractal order n increases, the HFC's space-filling performance within the BSC becomes better. Ignoring other effects, this allows more magnetic flux lines to intersect within the HFC region during the offset process, thereby increasing the mutual inductance between the coils and which in turn improves the TE of WPT system. On the other hand, higher order Hilbert curves to some extent confine the magnetic flux lines to a smaller area, which theoretically improves the TD of the coil. However, the higher order HFC structure requires relatively more wires for MCM, which also weakens the magnetic flux density in different directions, which sharply reduces the transmission performance of the coil.

To rigorously determine the impact of fractal order on coil performance, ANSYS-based simulations were conducted, yielding

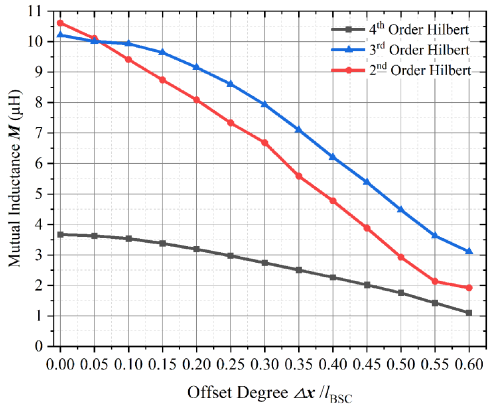

Fig. 3. Influence of Hilbert structures of different orders on the mutual inductance of coils.

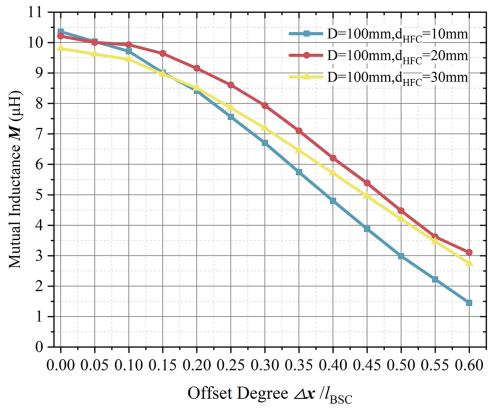

Fig. 4. Simulation results of coils mutual inductance for different d_{HFC}.

mutual inductance values across varying orders while maintaining constant d_{HFC} dimensions and total conductor length:

Analysis of Fig. 3 reveals that lower order Hilbert coil configurations exhibit higher mutual inductance during coaxial alignment. However, this advantage diminishes precipitously with increasing offset displacement. While higher order FC demonstrate significantly superior attenuation resistance in mutual inductance, their inherently lower baseline coupling renders them of limited practical utility.

Overall, this article proposes to use a third-order Hilbert curve as the structure of the HFC. By changing the size of d_{HFC}, the proportion of the HFC in coil can be changed. In order to further study the effect of the proportion of fractal structure in the coil on anti-offset performance, this article uses ANSYS to simulate and measure the mutual inductance of coils with different d_{HFC}, and the results are shown in Fig. 4.

The simulation data shows a conclusion similar to the Hilbert order. When the fractal structure accounts for a small proportion($d_{\mathrm{HFC}} = 10$ mm), its initial mutual inductance is slightly higher, but as the OD increases, its mutual inductance attenuation rate is greater. When the fractal structure accounts for a larger proportion ($d_{\mathrm{HFC}} = 30$ mm), its initial mutual inductance value is lower. Even though this design obtains a smaller mutual inductance attenuation rate, its application significance is not as good as the FC with $d_{\mathrm{HFC}} = 20$ mm. Therefore, the basic length of the FC designed in this article is $d_{\mathrm{HFC}} = 20$ mm.

Accordingly, the parametric configuration is fully determined by the structural characteristics of the Hilbert fractal as: $l_{\mathrm{HFC}} = 7d_{\mathrm{HFC}}$. All parameters in (12) are thus specified. Given the established Hilbert fractal geometry, a rectangular control coil with matching dimensions is designed, featuring an innermost tier comprising three turns. Consequently, its mutual inductance expression takes the form

$$M_0 = \sum_{i=1}^{m+3}\sum_{j=1}^{m+3} M_{\mathrm{ij}}. \tag{17}$$

For the rectangular coil configuration, where the side length a satisfies: $\max\{a_{\mathrm{m+1}}, a_{m+2}, a_{m+3}\} \le l_{\mathrm{HFC}}$

Thus, by mathematically subtracting common components from the mutual inductance expressions of both coil types while incorporating structural symmetry considerations, the refined expression resolves to

$$\Delta M_0(m, \Delta x, D) = 2\sum_{i=m+1}^{m+3}\sum_{j=1}^{m} M_{\mathrm{ij}} + M_{\mathrm{SS}} \tag{18}$$

in which

$$M_{\mathrm{SS}} = \sum_{i=m+1}^{m+3}\sum_{j=m+1}^{m+3} M_{\mathrm{ij}}$$

and

$$\Delta M_1(m,\Delta x,D) = 2\sum_{i=1}^{m} M_{\mathrm{SHi}} + M_{\mathrm{H}}. \tag{19}$$

The physical interpretation of both expressions encompasses the mutual inductance between inner-to-outer structures and inner-to-inner structural elements. Analyzing these equations while considering the geometric attributes reveals that traditional coils exhibit higher near-field magnetic flux concentration, facilitating greater mutual inductance during coaxial alignment. However, this advantage concurrently accelerates mutual inductance decay under offset conditions.

Conversely, fractal-structured coils demonstrate greater initial magnetic field dispersion with minimal distance-dependent variation. When subjected to offset, their inherent self-similarity ensures gradual mutual inductance attenuation and more uniform flux distribution.

To more comprehensively validate the coil's performance, this paper also compares the self-inductance of different coils via simulation. However, self inductance calculation for FC is highly complex, particularly for the HFC structure itself. Therefore, only the self-inductance results of conventional coils are presented.

Fig. 5 demonstrates the self-inductance variation patterns of various coils, which align with (15): the presence of HFC increases the coil fill factor, thereby reducing its self-inductance. It should be noted that the calculation formula does not account for the effects of Litz wire, leading to an underestimation of the actual r_0 value and consequently lower simulation results.

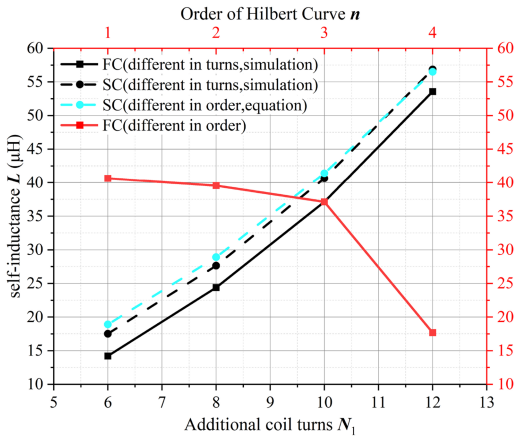

Fig. 5. Simulation results of coils' self-inductance.

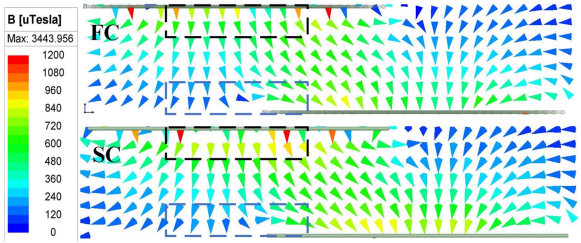

Fig. 6. Comparison of SC and FC magnetic field distribution ($\Delta x = 204$ mm).

When the coil length and area are held constant, the self-inductance of the FC proposed in this paper remains consistently approximately 3.5 μH lower than that of the conventional rectangular coil. Furthermore, from the perspective of fractal order, an increase in the fractal order results in a sharp decrease in the coil's self-inductance.This characteristic is also reflected in the size of the d_{HFC}: for coils wound with wires of the same length, the self-inductance is 38.478 μH when $d_{\mathrm{HFC}} = 10$ mm, 37.120 μH when $d_{\mathrm{HFC}} = 20$ mm, and 34.941 μH when $d_{\mathrm{HFC}} = 30$ mm. In other words, a larger proportion of the HFC region corresponds to a smaller self-inductance of the coil.

C. Performance Prediction of FC

On the basis of the determined $d_{\mathrm{HFC}} = 20$ mm, this paper sets up a SC with a length equal to it as a control group for FC.

Following the established parameters, the physical models of both coil types were initially constructed in ANSYS for electromagnetic simulation, from which preliminary mutual inductance values and magnetic field distributions were obtained. Subsequently, coil prototypes were fabricated accordingly, with their mutual inductances precisely characterized using a direct current resistance (DCR) bridge for experimental validation. Fig. 6 demonstrates the distinct magnetic field distribution disparities between FC and SC under lateral misalignment conditions.

The central region of Fig. 6 (FC) features an HFC structure. The difference between the magnetic fields generated by FC and SC is mainly due to two points: first, in the black area of the figure, FC has better spatial filling properties, which results in a more uniform distribution of the magnetic vector in the center; second, in the blue area of the figure, the FC coils have stronger constraints on the magnetic field in the misaligned area.

The simulated and measured mutual inductance comparisons between coil configurations are systematically presented in Fig. 7.

From the measurement results, it can be seen that the mutual inductance of both SC and FC will decrease rapidly when increasing with the OD and TD, but the mutual inductance between the two coils with the third-order HF structure has higher mutual inductance compared to SC. It is shown in the figure that at the initial state (or when the OD and TD are small), the mutual inductance value of SC will be superior to FC for a small segment of Δx and D increments, but as the amount of variation increases, the plotted SC mutual inductance surface will rapidly decrease below the FC mutual inductance surface.

From the OD Δx, within a certain offset range Δx_0, SC has higher initial mutual inductance than FC, but as the OD increases, the mutual inductance of SC will be inferior to that of FC when OD $\Delta x > \Delta x_0$. The mutual inductance between the two coils changes in the same trend, but the rate of change is slightly different: compared to SC, FC has a lower mutual inductance attenuation rate, especially when the OD Δx is 51–136 mm (i.e., 15% ~40% of the coil side length).

In terms of the TD D, SC has higher initial mutual inductance in most of the TD tested, while FC has higher initial mutual inductance than SC only at larger TD, and the mutual inductance of both decreases with the increase of D, and the difference between the two gradually decreases with the distance. But similarly, the SC advantageous OD Δx_0 will gradually decrease to 0 as the TD D increases, and this phenomenon also indicates that FC will have an overall advantage over SC in the case of longer TD. Both simulation and experimental results indicate that the mutual inductance values exhibit a consistent trend with minimal discrepancy. However, the measured self-inductance values are slightly higher than the simulation results. This deviation arises because approximately 1 m of additional wire was reserved for each coil to facilitate practical experimental connections. Consequently, a minor difference between the actual and expected self-inductance values is observed. Nonetheless, this discrepancy remains within a controllable range and does not materially impact the experimental outcomes.

Considering that the TE of a general WPT system is positively correlated with the mutual inductance of the coil, this also indicates that the coil structure proposed in this article has the potential to improve the TE of WPT system. In the process of practical application, it may be possible to highlight the FC advantage by increasing the TD, and at the same time increase the mutual inductance between the coils by using ferromagnetic materials.

In order to further verify the applicability of the coil proposed in this article, experiments will be conducted on the WPT system that only targets the specific structure of the coil. The schematic diagram of its experimental design is shown in Fig. 8.

U_{dc} is the dc input power, u_{in} is the ac output of the inverter, L_{f}, C_{f}, C_{T}, and C_{R} are the compensation inductance and compensation capacitance, $I_{\mathrm{T}}/I_{\mathrm{R}}$ are the current of transmitter and receiver, L_{T} and L_{R} are the self-inductance of the transmitter

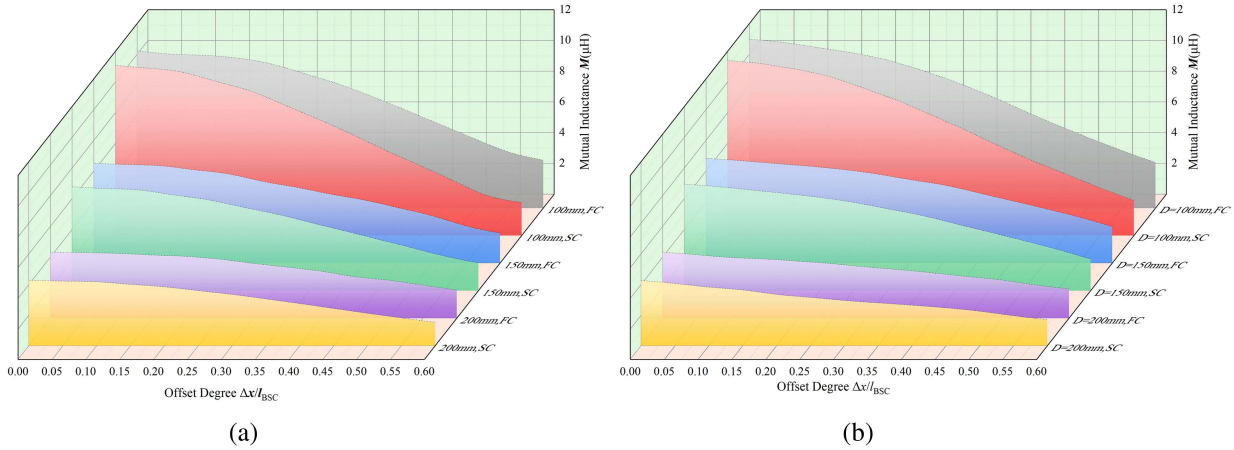

Fig. 7. Offset characteristic curve of coil mutual inductance. (a) Simulation results of mutual inductance. (b) Experiment results of mutual inductance.

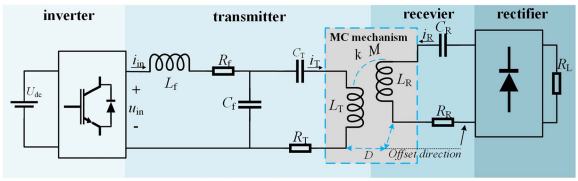

Fig. 8. Experimental circuit schematic.

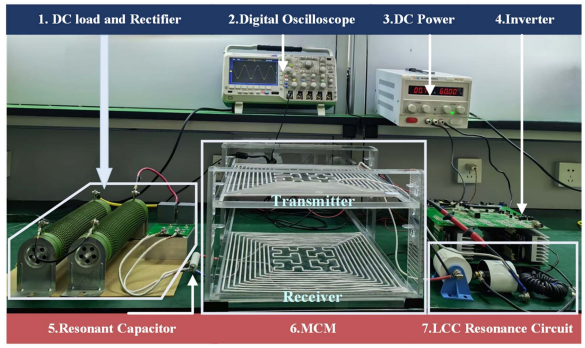

Fig. 9. Experimental verification device for proposed MCM.

and the receiver, R_{R} and R_{T} are the resistances of two coils, R_{f} is the compensation inductance and the equivalent resistance of the circuit wire, M is the mutual inductance of coils, k is the coupling coefficient of coils, and R_{L} is the load. The angular frequency of alternating current is $\omega = 2\pi f$.

Under full reactive power compensation, its efficiency expression can be written

$$\eta = \frac{\omega^2 M^2 R_{\mathrm{L}}}{(R_{\mathrm{L}} + R_{\mathrm{R}})(\omega^2 M^2 + R_{\mathrm{T}} R_{\mathrm{L}} + R_{\mathrm{T}} R_{\mathrm{R}})}. \tag{20}$$

III. Experimental Verification Based on WPT System

In order to further verify the conjecture, this chapter performs platform verification on MCM designed in this article. In order to avoid the influence of other factors on the transmission power of the system, the experimental platform adopts the *LCC-S* circuit topology with constant voltage input, without additional control means, and without the use of ferrites for magnetic conduction. Its experimental device is shown in Fig. 9.

Since all experimental circuits employed Litz wire, actual measurements revealed that the resistance values of R_{T}, R_{R}, and R_{f} were extremely small and could therefore be neglected. On this basis, the parameters of the components used in this experiment are shown in Table II.

Similar to the validation method described in Section II, the experiments in this chapter started with a set of PC plastic frames where the transmitter and receiver coils were placed parallel to each other at a distance of 120 mm. The PC plastic frame was equipped with a set of graduated sliding rails for moving the transmitter or receiver coils in parallel to simulate the coil offsets. Subsequently, the coils are offset along the slides in parallel according to the established offset scale, and an oscilloscope is used to measure the voltage across the resistors and observe the inverter output voltage and coil input voltage.

TABLE II
Experimental Component Parameters

Symbol	Value	Symbol	Value
L_{f}	15 μH	C_{f}	0.17 μF(SC)/0.16 μF(FC)
$L_{\mathrm{T}}/L_{\mathrm{R}}$(FC)	38.4 μH	C_{T}	0.08 μF
$L_{\mathrm{T}}/L_{\mathrm{R}}$(SC)	43.1 μH	C_{R}	0.047 μF
R_{L}	25Ω	U_{dc}	80 V(SC)/90 V(FC)

The input voltage and input current can be obtained directly from the dc power supply, and the transmission efficiency of the WPT system can be obtained by calculation

$$\eta = \frac{P_{out}}{P_{in}} \times 100\% = \frac{{U_{\mathrm{R_L}}}^2}{R_{\mathrm{L}} U_{\mathrm{dc}} I_{\mathrm{dc}}} \times 100\%. \tag{21}$$

The inverter output voltage and the transmitter input voltage when WPT system uses two coils are shown in Fig. 10. It can be clearly observed from the figure that both coils exhibit nearly identical phase shift angles, i.e., $\varphi_{\mathrm{SC}} \approx \varphi_{\mathrm{FC}}$, indicating that the circuits operate in relatively consistent ZVS states relative to the resonant point with both coils. This facilitates a more equitable comparison between the two coil types.

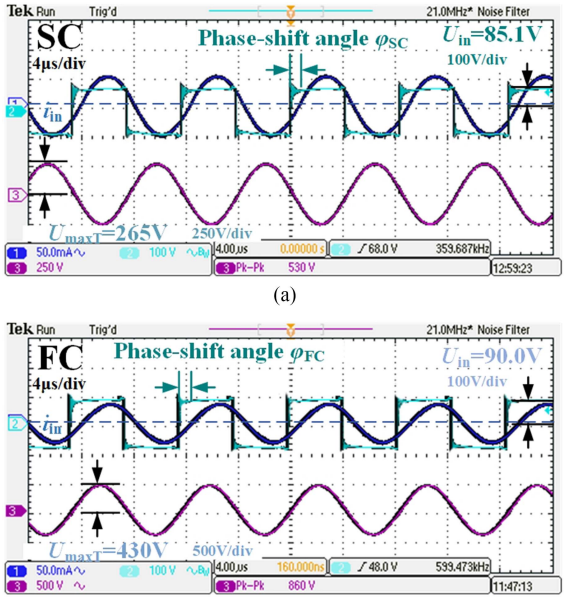

(a)

(b)

Fig. 10. Transmit coil input voltage waveform. (a) $U_{\rm in}$ and $U_{\rm LT}$ of SC. (b) $U_{\rm in}$ and $U_{\rm LT}$ of FC.

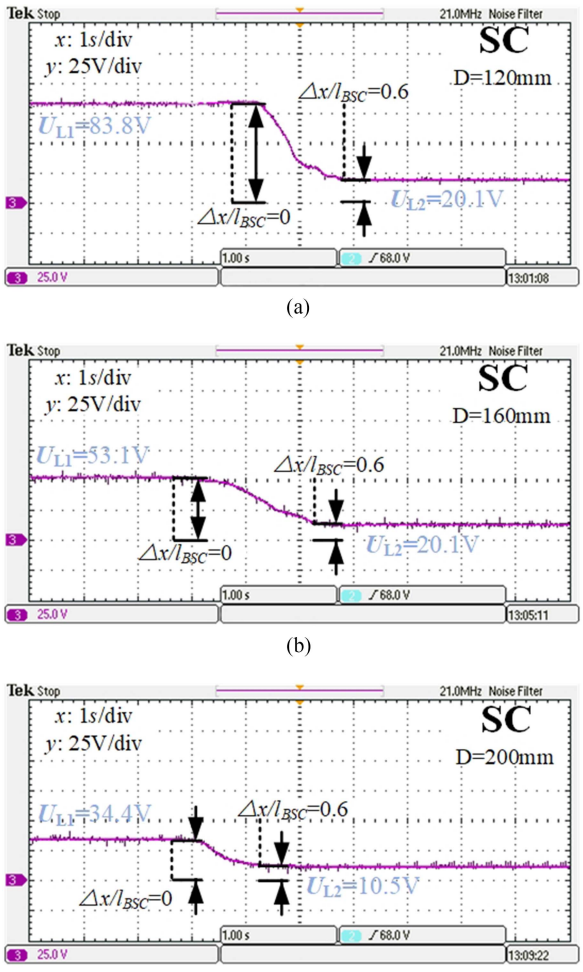

(a)

(b)

(c)

Fig. 11. Key experimental waveforms of SC in case of misaligned coils. (a) $D = 120$ mm. (b) $D = 160$ mm. (c) $D = 200$ mm.

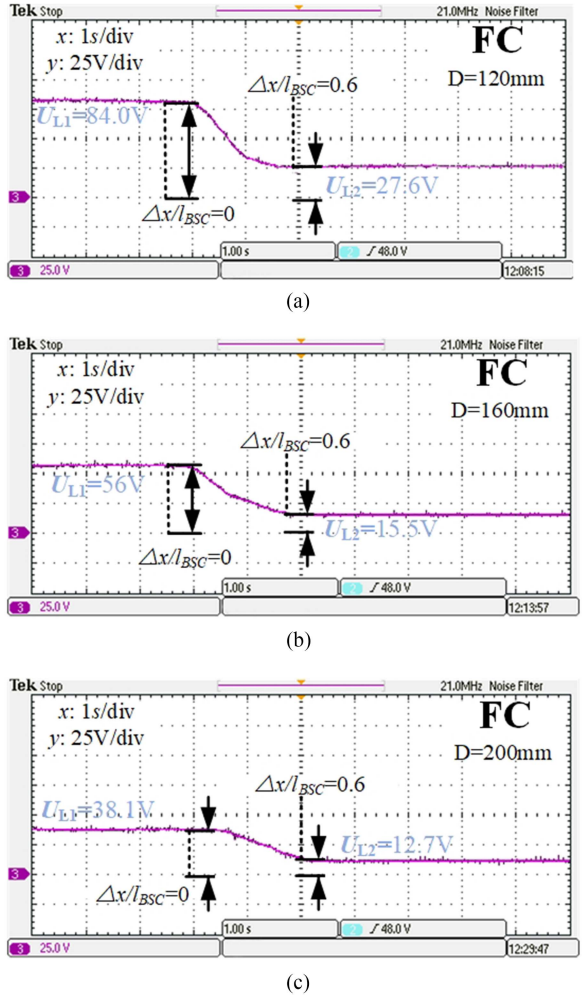

(a)

(b)

(c)

Fig. 12. Key experimental waveforms of FC in case of misaligned coils. (a) $D = 120$ mm. (b) $D = 160$ mm. (c) $D = 200$ mm.

Figs. 11 and 12 show the load voltage of the WPT system using SC and FC at different distances when continuously offset from $\Delta x = 0$ to $\Delta x = 204$ mm.

From the above waveforms, the following can be summarized.

1) In WPT system, the inverter output is a rectangular waveform with a frequency of 120 kHz, and the input voltage at the coil transmitter end is a sine waveform with a better 120 kHz waveform. When using FC, the peak $U_{\rm maxT}$ basically stabilizes at around 460 V, and when using SC, the peak $U_{\rm maxT}$ stabilizes at around 265 V.
2) During the experiment, the system input voltage and the emitter voltage basically remained constant. As the OD increased, the load voltage gradually decreased, and the circuit input current gradually decreased as well. This resulted in the overall system power gradually decreasing with the coil offset.
3) In the experiment, to verify the transmission performance and misalignment tolerance of the two types of coils, the input power supply was adjusted under the initial state ($\Delta x = 0, D = 120$ mm), achieving the same output power.

4) During the experiment, the system input voltage and transmitter terminal voltage remained largely constant. As the misalignment distance increased, the load voltage gradually decreased, accompanied by a corresponding reduction in the circuit input current. This resulted in a progressive decline in the overall system power as coil misalignment increased.

The experiment was conducted according to the design of the coil side length of 5% (17 mm) for a unit length of horizontal offset, and finally to the coil side length of 60% (204 mm) to stop, the purpose is to get the experimental results of the design of the coil is more guiding significance. Considering that the ripple will have a certain effect on the experimental results, the load voltage obtained from the experiment is chosen to be the effective value obtained within the sampling interval of the oscilloscope.

Fig. 13 shows the variations in load power and power decay rate during the experiment.

During the process of misalignment and increased TD, the FC demonstrated significantly superior stability in output power compared to SC, consistently maintaining higher output power throughout the experiment. Furthermore, the advantage of FC became more pronounced as the TD increased. This observation confirms two conclusions illustrated in Fig. 7: first, conventional coils exhibit significant performance degradation with misalignment in the near field; second, the confinement capability of magnetic fields in conventional coils weakens as TD increases.

For TD = 120 mm, the maximum power increase was 30.9 W, with a relative increase of 88.5% at maximum misalignment; similarly, for TD = 160 mm, it was 16.3 W and 64%, and for TD = 200 mm, 10.6 W and 46%

In terms of the power attenuation rate, a particularly distinct interval exists on all three transmission distances at approximately $\Delta x = 85 \sim 119$ mm (25% $\sim$ 35% of the side length), where the increasing trend of the FC attenuation rate is very slow and even decreases to some extent. This is because at a misalignment distance of 100 mm, the HFC region and BSC region constitute the primary overlapping parts, and within this misalignment range, the advantage of FC is fully demonstrated. This will also be verified in the subsequent analysis of efficiency results.

The final result of efficiency is shown in Fig. 14.

In order to show more intuitively the performance improvement of FC relative to SC in the offset case, the efficiency increment between the two is denoted by $\Delta\eta = \eta_{\mathrm{FC}} - \eta_{\mathrm{SC}}$, and the result of its variation with OD is shown in Fig. 15.

FC exhibits a significantly superior advantage compared to SC. Under identical operating conditions, the FC coil remarkably improves the coil's misalignment tolerance.

From an overall point of view, TE change rule shown in Fig. 14 is basically consistent with the change rule of mutual inductance shown in Fig. 7. Although SC exhibits a marginal advantage in the near-field under minor misalignments, FC demonstrates absolute superiority both with increasing misalignment degrees and TD: first, as misalignment intensifies, FC significantly outperforms SC in both power and efficiency; second, with increasing TD, FC not only maintains this advantage but also relatively extends its lead. These findings align with the anticipated experimental outcomes.

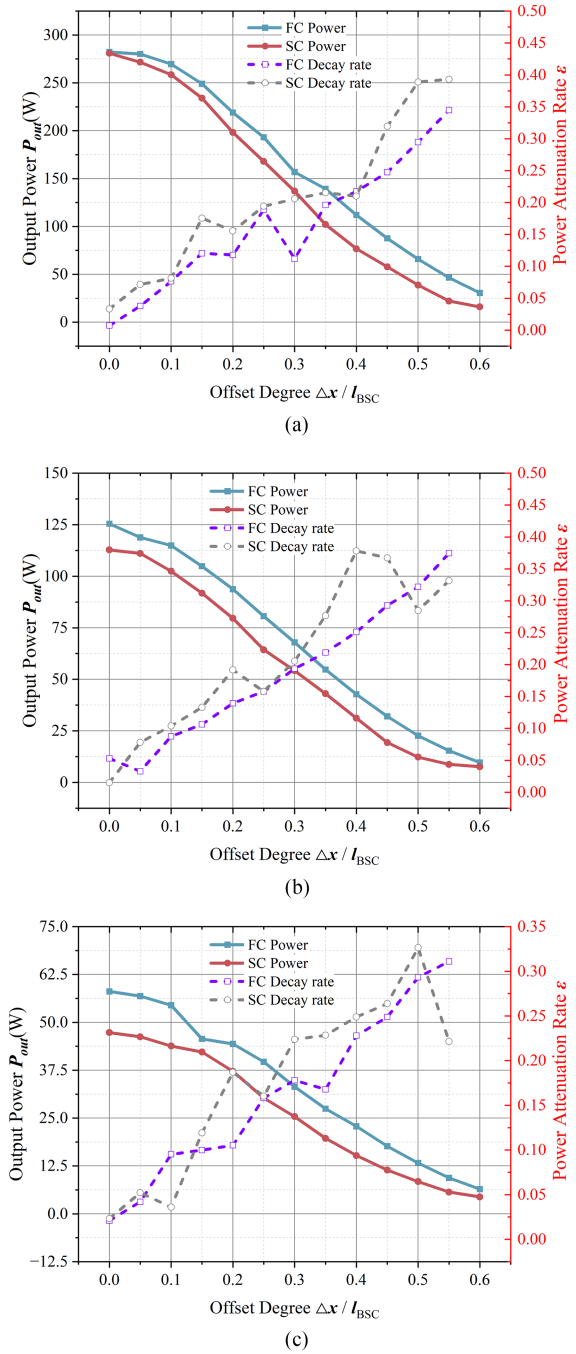

Fig. 13. Output power result of the offset experiment on WPT system. (a) $D = 120$ mm. (b) $D = 160$ mm. (c) $D = 200$ mm.

Fig. 15 highlights two intervals within which the efficiency difference between FC and SC reaches peak values. However, this peak difference diminishes as TD increases. It is noteworthy that the characteristic exhibited by this peak value also corresponds with the power decay rate of the coils shown in Fig. 13.

When TD = 120 mm, FC achieves an efficiency improvement of up to 23.79% relative to SC. At TD = 160 mm, the maximum

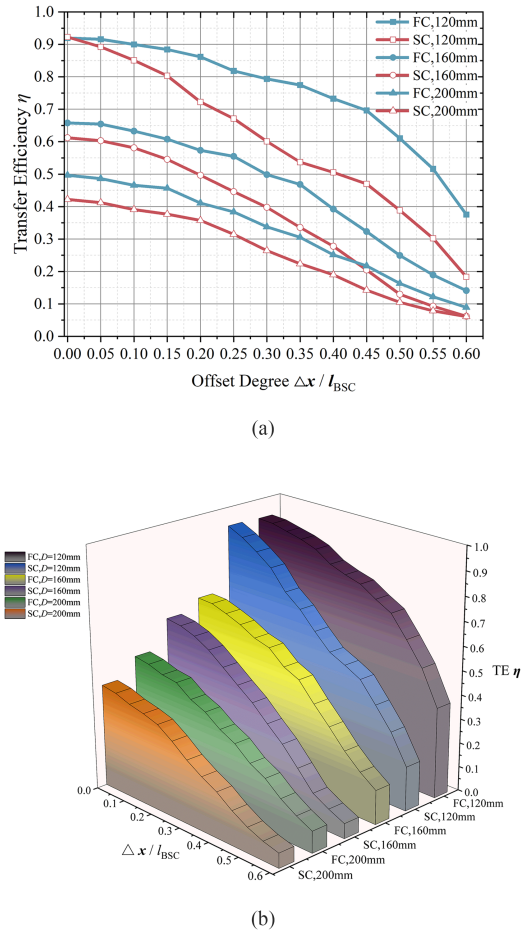

Fig. 14. TE result of the offset experiment on WPT system. (a) Two-dimensional view. (b) Three-dimensional view.

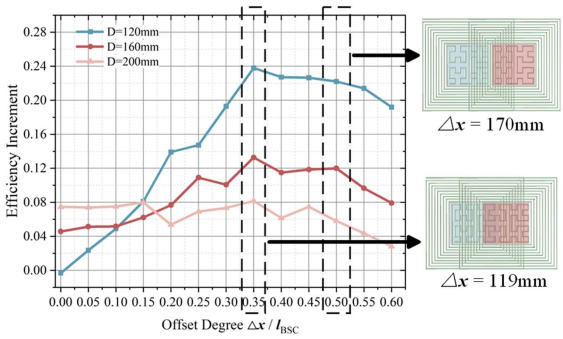

Fig. 15. Efficiency increment of MCM offset experiment.

efficiency improvement is 13.27%, while at TD = 200 mm, efficiency is enhanced by up to 8.15%. However, it should be noted that as TD increases, the advantage of the FC coil diminishes under significant misalignments. This occurs because both coil types exhibit poor coupling effects in such extreme scenarios.

In Section II-B, (19) the advantage of FC stems from the greater misalignment resistance of M_{SHi}. compared to M_{ij}, enabling it to achieve higher power or efficiency during misalignment. In Section II-A, (14), M_{ij} provides the coils with a sufficiently large fundamental mutual inductance, ensuring that FC maintains a comparable baseline to SC. Under the influence of the fractal structure, M_{H}, M_{SHi}, and M_{HSj} exhibit superior robustness. The experimental conclusions align well with the theoretical foundation presented earlier.

Synthesizing the experimental results, the advantages of the FC coil over the SC are primarily concentrated in two aspects. First, during coil misalignment, the WPT system using the FC coil achieves higher transmission efficiency than the system using the SC coil. This advantage stems from the better magnetic field confinement demonstrated by the HFC region in Fig. 6. Second, even in the absence of misalignment but at larger TD, WPT system employing the FC coil can achieve improved efficiency. This benefit originates from the more concentrated magnetic field within the HFC region shown in Fig. 6.

In practical applications, the dual advantages of FC can bring good application prospects: for example, in the wireless charging application of EVs, when charging in parking, the anti-misalignment advantage of FC coils can reduce the waste of energy brought about by parking to the inadmissible charging area, and at the same time for different chassis heights of the car also has a better compatibility.

To delineate the unique attributes of this research within the current landscape—particularly compared with RC implementations and multicoil superposition approaches cited in the Section I—Table III presents a unified cost analysis of coil designs across relevant literature. For performance normalization, Table IV benchmarks system efficiency metrics at 30% lateral offset relative to each coil's maximum dimension.

IV. Conclusion

This article is based on Hilbert curves and summarizes the advantages and disadvantages of Hilbert curves in the design of information security structures by referring to the application of Hilbert fractal curves in other fields. A rectangular coil with a Hilbert curve structure is designed. On the basis of not using additional coils and not increasing additional costs, the performance of the coil has been comprehensively improved. This represents a transformative departure from current research paradigms that rely solely on SC permutations for structural modifications.

This article demonstrates that the proposed fractal-shaped coil exhibits significantly enhanced misalignment tolerance compared to conventional rectangular coils under substantial lateral offsets at close-range TD, thereby providing an effective solution to the misalignment issue in wireless charging coupling mechanism design for EVs. Furthermore, the proposed coil configuration demonstrates maintained performance resilience against extended TD, indicating its potential suitability for EVs with varying chassis heights.

Since all current studies based on coil structures basically use the SC structure referenced in this article [4], [8], [13], [17], [18], [19], [21], the coil proposed in this article has achieved an improvement in the transmission performance of WPT system by simply changing the coil structure while maintaining the same economic benefits. This has great reference significance for research in related fields.

TABLE III
COMPARATIVE COST ANALYSIS OF COIL DESIGNS

Reference	Circuit	Tx (mm)	Rx (mm)	RC (mm)	Extra Components	Extra Cost
[34]	S-S	400*400	400*400	600*600	RC and Ferrite	Medium
[35]	LCC-LCC	150*150	150*150	None	DD Tx	Low
[24]	S-S	393*493	297*347	648*468	RC	Medium
[26]	S-S	200*200	200*200	200*80	4 RC and Ferrite	High
[25]	S-S	480*380	480*380	738*638	RC,Ferrite and Al plate	High
This paper	LCC-S	340*340	340*340	None	None	None

TABLE IV
EXPERIMENTAL COIL PERFORMANCE COMPARISON

Reference	Power (W)	Maximum Efficiency	Transfer Distance (mm)	Performance
[34]	1000	92.1%	200	3% enhancement over conventional rectangular coils
[35]	150	87.2%	40	Efficiency: 47.5%
[24]	63.1∼71.9	91.6%	150	Efficiency stabilized around 91%
[26]	105	86%	100	Efficiency: approximately 81%
[25]	4000	95.83%	150	Not mentioned
This paper	300	91.95%	120/160/200	Effciency: 79.37%/49.85%/33.76%

Regarding the investigation of FC, this article does not propose a generalized design methodology. Research on the optimization of coil structures may be more effectively advanced in the future through deep learning or artificial intelligence techniques [35].

REFERENCES

[1] Z. Dai, J. Wang, H. Zhou, and H. Huang, "A review on the recent development in the design and optimization of magnetic coupling mechanism of wireless power transmission," *IEEE Syst. J.*, vol. 14, no. 3, pp. 4368–4381, Sep. 2020.

[2] E. Moisello, A. Liotta, P. Malcovati, and E. Bonizzoni, "Recent trends and challenges in near-field wireless power transfer systems," *IEEE Open J. Solid-State Circuits Soc.*, vol. 3, pp. 197–213, 2023.

[3] Y. Yao, P. Sun, X. Liu, Y. Wang, and D. Xu, "Simultaneous wireless power and data transfer: A comprehensive review," *IEEE Trans. Power Electron.*, vol. 37, no. 3, pp. 3650–3667, Mar. 2022.

[4] B. Luo, T. Long, R. K. Mai, R. M. Dai, Z. Y. He, and W. H. Li, "Analysis and design of hybrid inductive and capacitive wireless power transfer for high-power applications," *IET Power Electron.*, vol. 11, no. 14, pp. 2263–2270, 2018.

[5] V. Ramakrishnan et al., "A comprehensive review on efficiency enhancement of wireless charging system for the electric vehicles applications," *IEEE Access*, vol. 12, pp. 46967–46994, 2024.

[6] S. J. Zhao, F. W. Chen, C. S. Tang, P. Q. Deng, and C. Z. Duan, "Modeling and control of WPT systems in the presence of load and mutual inductance variations," *IEEE Trans. Power Electron.*, vol. 39, no. 11, pp. 15315–15328, Nov. 2024.

[7] X. Lu, P. Wang, D. Niyato, D. I. Kim, and Z. Han, "Wireless charging technologies: Fundamentals, standards, and network applications," *IEEE Commun. Surv. Tut.*, vol. 18, no. 2, pp. 1413–1452, Secondquarter 2016.

[8] Y. H. Jia, L. Zhao, Z. H. Wang, C. S. Tang, F. W. Chen, and H. Feng, "Integrated LCC-LCC topology for WPT system with CC output regarding air gap and load variations," *IEEE Trans. Power Electron.*, vol. 39, no. 10, pp. 11904–11915, Oct. 2024.

[9] D. Shen, G. Du, W. Zeng, Z. Yang, and J. Li, "Research on optimization of compensation topology parameters for a wireless power transmission system with wide coupling coefficient fluctuation," *IEEE Access*, vol. 8, pp. 59648–59658, 2020.

[10] X. Liu et al., "A multi-inverter multi-rectifier wireless power transfer system for charging stations with power loss optimized control," *IEEE Trans. Power Electron.*, vol. 38, no. 8, pp. 9261–9277, Aug. 2023.

[11] M. Wang, G. Song, R. Yin, and Y. Shi, "Design and analysis of an anti-misalignment wireless power transfer system," *IEEE Microw. Wireless Compon. Lett.*, vol. 33, no. 2, pp. 228–231, Feb. 2023.

[12] Y. Chen, S. He, B. Yang, S. Chen, Z. He, and R. Mai, "Reconfigurable rectifier-based detuned series-series compensated IPT system for anti-misalignment and efficiency improvement," *IEEE Trans. Power Electron.*, vol. 38, no. 2, pp. 2720–2729, Feb. 2023.

[13] J. Mai et al., "A novel rectifier for decoupled DD pads in electric vehicle WPT system with high misalignment tolerance and interoperability," *IEEE Trans. Power Electron.*, vol. 40, no. 10, pp. 14337–14342, Oct. 2025.

[14] H. Zhao et al., "Nonresonant compensation optimization for efficiency improvement of wireless power transfer system with relay coil," *IEEE Trans. Power Electron.*, vol. 39, no. 2, pp. 2835–2845, Feb. 2024.

[15] C. Rong et al., "Optimized design of passive array coils for high-efficiency and anti-misalignment WPT system," *IEEE Trans. Power Electron.*, vol. 39, no. 5, pp. 6504–6514, May 2024.

[16] H. Zhou, Z. Shen, Y. Wu, Y. Zhuang, and Y. Zhang, "An anti-misalignment wireless charging system for low-power applications based on solenoid coils incorporated with reverse windings," *IEEE Trans. Consum. Electron.*, vol. 70, no. 1, pp. 371–377, Feb. 2024.

[17] Z. Liu, Z. Chen, and J. Li, "A magnetic tank system for wireless power transfer," *IEEE Microw. Wireless Compon. Lett.*, vol. 27, no. 5, pp. 443–445, May 2017.

[18] R. Mai, B. Yang, Y. Chen, N. Yang, Z. He, and S. Gao, "A misalignment tolerant IPT system with intermediate coils for constant-current output," *IEEE Trans. Power Electron.*, vol. 34, no. 8, pp. 7151–7155, Aug. 2019.

[19] M. Wu et al., "A compact coupler with integrated multiple decoupled coils for wireless power transfer system and its anti-misalignment control," *IEEE Trans. Power Electron.*, vol. 37, no. 10, pp. 12814–12827, Oct. 2022.

[20] H. Wang, Y. Wu, X. Li, X. Dai, Y. Sun, and J. Hu, "Advanced magnetic coupler design with multi-directional anti-misalignment capabilities for wireless charging unmanned aerial vehicles," *IEEE Trans. Circuits Syst. II Exp. Briefs*, vol. 71, no. 6, pp. 3231–3235, Jun. 2024.

[21] P. Cao et al., "A new hybrid magnetic coupler in inductive power transfer system for high misalignment tolerance," *IEEE Access*, vol. 12, pp. 72187–72198, 2024.

[22] P. Darvish, H. Cao, M. F. Uddin, H. Wang, and Y. Zhao, "A generic coupled and/or decoupled integrated inductors optimization for WPT applications," *IEEE Trans. Power Electron.*, vol. 40, no. 10, pp. 15976–16003, Oct. 2025.

[23] M. Wolf and D. Shmilovitz, "Substantial reduction of solenoidal ferrite rod coil losses through winding geometry modification," *IEEE Trans. Magn.*, vol. 60, no. 9, Sep. 2024, Art. no. 8401305.

[24] Z. Li, J. Li, S. Li, Y. Yu, and J. Yi, "Design and optimization of asymmetric and reverse series coil structure for obtaining quasi-constant mutual inductance in dynamic wireless charging system for electric vehicles," *IEEE Trans. Veh. Technol.*, vol. 71, no. 3, pp. 2560–2572, Mar. 2022.

[25] Z. Li, W. Zhang, Z. Gan, and B. Li, "Study on composite structure of tian-font magnetic shielding and anti-series active coils for wireless power transfer system," *CPSS Trans. Power Electron. Appl.*, vol. 10, no. 1, pp. 97–109, 2025.

[26] P. Yadav and M. Veerachary, "Modified coupler with reduced misalignment issues for wireless power transfer system," *IEEE Trans. Ind. Appl.*, vol. 60, no. 4, pp. 5763–5777, Jul./Aug. 2024.

[27] C. Zhang, W. Wang, C. Xu, and J. Yang, "Research on uniform magnetic field compensation structure of array circular coils for wireless power transfer," *IEEE Trans. Magn.*, vol. 57, no. 6, Jun. 2021, Art. no. 8600205.

[28] F. Tian, A. Jiang, T. Yang, J. Qian, R. Liu, and M. Jiang, "Application of fractal geometry in gas sensor: A review," *IEEE Sens. J.*, vol. 21, no. 13, pp. 14587–14600, Jul. 2021.

[29] J. Tian et al., "Design of a flexible UHF Hilbert antenna for partial discharge detection in gas-insulated switchgear," *IEEE Antennas Wirel. Propag. Lett.*, vol. 22, no. 4, pp. 794–798, Apr. 2023.
[30] R. Wang, P. Guo, L. Wang, and Z. Xu, "Serpentine antenna with Hilbert unit for corona discharge detection," *IEEE Sens. J.*, vol. 24, no. 20, pp. 32334–32342, Oct. 2024.
[31] Z. Xu and G. Hei, "Rectangular spiral antenna with a Hilbert unit for detecting corona discharge in overhead lines," *IEEE Sens. J.*, vol. 21, no. 2, pp. 930–936, Jan. 2021.
[32] U. Ali et al., "A novel fractal Hilbert curve-based low-cost and highly sensitive microwave sensor for dielectric characterization of liquid materials," *IEEE Sensors J.*, vol. 23, no. 20, pp. 23950–23957, Oct. 2023.
[33] L. Yousefi and O. M. Ramahi, "Artificial magnetic materials using fractal Hilbert curves," *IEEE Trans. Antennas Propag.*, vol. 58, no. 8, pp. 2614–2622, Aug. 2010.
[34] G. Wei, J. Feng, J. Zhang, C. Wang, C. Zhu, and S. Y. Ostanin, "An efficient power and data synchronous transfer method for wireless power transfer system using double-D coupling coil," *IEEE Trans. Ind. Electron.*, vol. 68, no. 11, pp. 10643–10653, Nov. 2021.
[35] Fawad, S. A. A. Shah, Y. Park, and Y. S. Kim, "Machine learning-driven joint structuring of WPT coil and core for enhanced mutual inductance and reduced ferrite volume," *IEEE Trans. Power Electron.*, vol. 40, no. 10, pp. 15880–15890, Oct. 2025.

Zhiying Zheng was born in Yichang, China, in 2002. He received the B.S. degree in electrical engineering in 2024 from Naval University of Engineering, Wuhan, China, where he is currently working toward the Ph.D. degree in electrical engineering.

His current research interests include wireless power transfer and system modeling.

Zhihao Ye received the B.S., M.Sc., and Ph.D. degrees in electrical engineering from the Naval University of Engineering, Wuhan, China, in 1997, 2000 and 2005, respectively.

He is currently a Professor of electrical engineering with Naval University of Engineering. He was a Professor with the Naval Engineering Power Electronics Technology Institute, in 2012. His research interests include power system analysis, wireless power transfer, integrated power system and power system fault diagnosis.

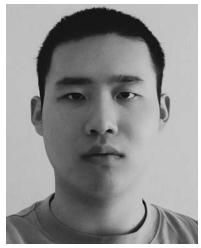

Changcheng Zhao received the B.S. degree in electrical engineering in 2024 from Naval University of Engineering, Hubei, China, where he is currently working toward the master's degree in electrical engineering.

His main research interests concentrate on wireless power transfer and system identification.

Cheng Chen received the B.S. degree in mechanical engineering from the Wuhan Institute of Bioengineering, Wuhan, China, in 2012, and the M.S. degree in control engineering and the Ph.D. degree in mechatronic engineering from Wuhan University, Wuhan. China, in 2015 and 2019, respectively.

In 2019, he joined Naval University of Engineering, where he is currently an Associate Professor. His research interests include wireless power transfer, system modeling, nonlinear control, and power system fault diagnosis.

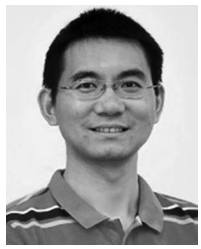

Qijun Deng received the B.S and M.Sc. degrees in mechanical engineering and the Ph.D. degree in computer application technology from Wuhan University, Wuhan, China, in 1999 and 2002, 2005 respectively.

In 2005, he joined the Department of Automation (which was merged into School of Electrical Engineering and Automation in 2018, and Robotics School in 2025, respectively), Wuhan University, where he is currently a Professor. From 2013 to 2014, he was a Visiting Scholar with the New York University Tandon School of Engineering, Ner York, NY, USA. His research interests include wireless power transfer, distribution automation, and electrical power informatics.